# Tilted and nontilted Ag overlayer on a Ni(111) substrate: Structure and energetics

Carole Chambon,[1,2] Jérôme Creuze,[3] Alessandro Coati,[1] Michèle Sauvage-Simkin,[1] and Yves Garreau[1,2]
[1]*Synchrotron SOLEIL, L'Orme des Merisiers, Saint Aubin, BP 48, F91192 Gif sur Yvette Cedex, France*
[2]*MPQ, Université Denis Diderot Paris VII, Bât. Condorcet, Case courrier 7021, F75205 Paris Cedex 13, France*
[3]*LEMHE/ICMMO, Université Paris Sud-XI, UMR8182, Bât. 410, F91405 Orsay Cedex, France*
(Received 5 December 2008; revised manuscript received 18 January 2009; published 6 March 2009)

The first stages of silver growth on a nickel (111) surface, for coverages up to 2 monolayers, have been investigated by quenched molecular dynamics (QMD) simulations and low energy electron diffraction (LEED). After a thermal treatment, a collinear $(7\times7)$ reconstruction, with $Ag(111)\|Ni(111)$ and $Ag[1\bar{1}0]\|Ni[1\bar{1}0]$, observed at room temperature, is seen to change into a tilted reconstruction where the silver lattice is rotated by $2.4\pm0.4°$ with respect to the substrate, the new cell dimensions being close to the $(7\times7)$ ones. In order to determine the geometry of this kind of tilted but still commensurate reconstruction, we have generated a large number of solutions with a rotation of the silver layer from 1° to 40° with respect to the substrate. The adsorption energies calculated by QMD simulations have shown that three of those tilted reconstructions, corresponding, respectively, to rotation angles equal to 1°, 2.2°, and 3.5°, are energetically more stable than the collinear one. These results support not only the present LEED data but also the tilted superstructures observed by various authors using LEED or scanning tunneling microscopy.

DOI: 10.1103/PhysRevB.79.125412 PACS number(s): 68.35.bd, 68.35.Ct, 68.47.De

## I. INTRODUCTION

Metal-on-metal growth is now a long-established and extensively studied phenomenon, at least for substrates with low Miller index orientations.[1,2] Based on the common epitaxial relationships, i.e., the alignment of the close-packed rows in both metals, and the so-called wetting energy, these pioneering works allow one to predict the growth mode of a thin heteroepitaxial film.[2,3] Moreover, in the case of two metals with the same crystallographic structure but with different lattice parameters, the misfit leads to the well-known moiré effect. We consider here the Ni-Ag system, which belongs to the class of alloys with a strong tendency to phase separation in the bulk[4,5] and with a large lattice parameter mismatch (16%).[6] Moreover, silver is less cohesive than nickel ($E_{coh}^{Ag}=-2.95$ eV and $E_{coh}^{Ni}=-4.44$ eV), leading, when one considers the atomic size difference and the very weak solubility limits, to Ag segregation at the surface and thus to the formation of an abrupt interface. Therefore, Ag/Ni can be considered as a model system for the study of metal-on-metal growth mechanism.

The Ag/Ni(111) interface formation has been investigated by a large variety of surface science tools: Auger electron spectroscopy (AES) and low-energy electron diffraction (LEED),[7–13] photoelectron spectroscopy (PES),[14–17] time-of-flight impact-collision ion scattering spectroscopy (TOF-ICISS),[13,18] and scanning tunneling microscopy (STM).[19–21] The main purpose of these investigations is the understanding of the growth mechanism of Ag on Ni surfaces in the early stages and its dependence on the thermal conditions both for deposition and postgrowth treatments. The compilation of the published data, together with our own findings described below, reveals that several epitaxial relationships between the thin silver adlayer and the Ni(111) substrate may occur. In particular, LEED studies have revealed a structural phase transition in the Ag/Ni(111) interface as a function of annealing temperature: from room temperature (RT) up to a given temperature (different according to the various authors[7,9,12]), the Ag overlayer adopts a hexagonal packing with the dense directions parallel to those of the nickel substrate leading to a collinear $(7\times7)$ or $(6\times6)$ interface supercell. Above the transition temperature, double spots appear, corresponding to two tilted domains with an angular deviation from $\pm1°$ to $\pm3°$ between the crystal lattices of the two materials. More recent STM data[19,20] present two different noncollinear moiré patterns.

Many other adsorption systems coupling hexagonal monolayer structures with substrates of hexagonal surface symmetry exhibit the same interesting behavior of rotational epitaxy,[22–27] and several theoretical models have been proposed to describe them. Indeed, the Novaco-McTague model[28,29] is the most well-known and accepted one. It describes the monolayer in terms of its elastic constants and shows that the ground state of an adsorbed monolayer could be at a nonsymmetry angle with respect to the substrate. However, the interaction between the substrate and the adsorbed layer is assumed to be very weak and thus the rotational epitaxy is mainly driven by the adsorbate-adsorbate interactions. Other models have been proposed since the pioneering work of Novaco and McTague[28] based on symmetry considerations[30] or using a single Fourier component expansion for the adsorbed atom interaction with the surface.[31] Recently, Tkatchenko[32,33] developed an analytical theory in which the interaction potential is described by a Fourier series with up to six shells of reciprocal lattice vectors. The main conclusion arising from this study is that an accurate description of the adsorbate-substrate interaction is needed for a quantitative theory of such phenomenon, i.e., *ab initio* calculations of the Fourier coefficients for different complex adsorption systems. Even if this model is able to describe very different types of adsorbate-substrate interactions in principle, the actual determination of the Fourier coefficients may not be straightforward, especially when large relaxations occur in the substrate as is the case for metal-on-metal growth.

 

Therefore, to go deeper into the understanding of the stabilization of the various tilted superstructures obtained for the Ag/Ni(111) interface, we have performed atomic-scale simulations with realistic *N*-body potentials derived from the electronic structure; an approach which has proved very efficient to interpret metal-on-metal reconstruction in a variety of systems.[34–37] It is the purpose of the present paper to produce a reliable energy scale for the different superstructures and to confront our results with the available corpus of experimental data.

The paper is organized as follows: the experimental procedure is described in Sec. II and the different theoretical tools used in this study are summarized in Sec. III. In Sec. IV, we present our results and their analysis. Finally, we draw our conclusions in Sec. V.

## II. EXPERIMENTAL

The substrate is a Ni single crystal ($4\times4$ mm$^2$), with a (111) polished surface. After the introduction in a UHV chamber ($2\times10^{-10}$ mbar) connected with an experimental setup hosting an Omicron VT-STM, the surface was cleaned by repeated cycles of sputtering with 1 keV Ar ions and flash annealing at approximately 1000 K. AES was used to check the absence of contaminants (C, O,…). STM allowed us to characterize the surface morphology,[21] whereas the surface crystallographic structure was studied by LEED performed at room temperature. STM imaging of surfaces (not shown here) has revealed large flat terraces separated by steps of $(2.0\pm0.2)$ Å height, corresponding to a Ni monoatomic step (2.03 Å). The sample presented an irregular distribution of terrace widths (1 $\mu$m for the largest ones).

Silver atoms were deposited on the clean Ni surface by means of an electron gun evaporator (Omicron-EFM3). The deposition rate was 0.07 monolayer (ML)/min. Note that 1.0 ML is defined here as the quantity of Ag that is required to cover all the Ni(111) surface with a film of one Ag atomic layer height. Ag deposits from 0.1 to 2.2 ML were performed at RT or at 400 K, followed by thermal annealing in order to study the Ag organization on the surface. The annealing was interrupted when a thermocouple located close to the sample reached the desired temperature. The lateral homogeneity of the deposits on the sample surface was checked by AES, STM, and LEED measurements.

## III. COMPUTATIONAL

### A. Commensurate overlayer construction

In order to determine the relative stability of the different superstructures, we have used the commensurate monolayer construction proposed by Tkatchenko,[33] which determines all the possible coincidence lattices of a hexagonal monolayer deposited on top of a substrate with hexagonal symmetry. In fact, any expanded hexagonal nonprimitive cell can be obtained starting from a simple geometrical description of the substrate, in which the (111) plane is spanned by two vectors $\boldsymbol{a}$ and $\boldsymbol{b}$, with $\|\boldsymbol{a}\|=\|\boldsymbol{b}\|$ and $(\widehat{\boldsymbol{a},\boldsymbol{b}})=120°$. Any such nonprimitive cell can be written as a linear combination of the $\boldsymbol{a}$ and $\boldsymbol{b}$ vectors and it can be defined by a set of vectors $\boldsymbol{A}$ and $\boldsymbol{B}$, with $\boldsymbol{A}=(m\boldsymbol{a},n\boldsymbol{b})$ and $\boldsymbol{B}=(m\boldsymbol{b},-n(\boldsymbol{a}+\boldsymbol{b}))$, where $m$ and $n$ are integers. Those two vectors $\boldsymbol{A}$ and $\boldsymbol{B}$ have the same properties than $\boldsymbol{a}$ and $\boldsymbol{b}$, $\|\boldsymbol{A}\|=\|\boldsymbol{B}\|$ and $(\widehat{\boldsymbol{A},\boldsymbol{B}})=120°$. Therefore, the nonprimitive cell multiplicity (i.e., the number of lattice sites) is given by $N=m^2+n^2-mn$.

Using this construction, any hexagonal commensurate adlayer-substrate configuration can then be easily described. The adsorbate lattice is defined by the two vectors $\boldsymbol{A}_{\mathrm{ads}}=(m_a\boldsymbol{a}_{\mathrm{ads}},n_a\boldsymbol{b}_{\mathrm{ads}})$ and $\boldsymbol{B}_{\mathrm{ads}}=(m_a\boldsymbol{b}_{\mathrm{ads}},-n_a(\boldsymbol{a}_{\mathrm{ads}}+\boldsymbol{b}_{\mathrm{ads}}))$, and the substrate lattice by $\boldsymbol{A}_{\mathrm{sub}}=(m_s\boldsymbol{a}_{\mathrm{sub}},n_s\boldsymbol{b}_{\mathrm{sub}})$ and $\boldsymbol{B}_{\mathrm{sub}}=(m_s\boldsymbol{b}_{\mathrm{sub}},-n_s(\boldsymbol{a}_{\mathrm{sub}}+\boldsymbol{b}_{\mathrm{sub}}))$, where $m_a$, $n_a$, $m_s$, and $n_s$ are integers. The adlayer-substrate coincidence lattice is obtained by setting $\boldsymbol{A}_{\mathrm{ads}}=\boldsymbol{A}_{\mathrm{sub}}$ and $\boldsymbol{B}_{\mathrm{ads}}=\boldsymbol{B}_{\mathrm{sub}}$, which leads, in most cases, not only to rotate the adsorbate lattice but also to dilate or compress it depending on the residual mismatch. Indeed, the moiré structure does not compulsory follow the close-packed rows of the adsorbate and substrate lattices. At this stage, one introduces two characteristic parameters: the tilt angle $\alpha$ between the adsorbate and substrate lattice vectors and the rotation angle $\theta$ of the moiré structure which are, respectively, given by $\alpha=(\widehat{\boldsymbol{a}_{\mathrm{sub}},\boldsymbol{a}_{\mathrm{ads}}})$ and $\theta=(\widehat{\boldsymbol{a}_{\mathrm{sub}},\boldsymbol{A}_{\mathrm{sub}}})$.

Then the numbers of adsorbate atoms and of substrate atoms are, respectively, given by $N_{\mathrm{ads}}=m_a^2+n_a^2-m_an_a$ and $N_{\mathrm{sub}}=m_s^2+n_s^2-m_sn_s$. Thereby, we get a commensurate structure with the interface density ratio, $\tau$, given by

$$\tau=\frac{N_{\mathrm{ads}}}{N_{\mathrm{sub}}}. \tag{1}$$

It is worth noticing that to a given number of atoms $N=m^2+n^2-mn$ ($m,n$ integers) may correspond different $(m,n)$ couples and thus different $\boldsymbol{A}$ and $\boldsymbol{B}$ construction vectors with the same norms (i.e., different $\alpha$ and $\theta$ angles).

### B. Derivation of a *N*-body potential for Ag-Ni system

The interatomic potentials used in this study are derived from the second-moment approximation (SMA) of the tight-binding scheme.[38,39] These potentials have been quite successful in the calculation of bulk,[38] surface,[36,37,40–44] and grain boundary[41,45–47] equilibrium configurations for both pure metals and binary alloys.[48] The total energy $E_i$ at each site $i$ is written as a sum of a many-body attractive band term and a pairwise repulsive term:[38]

$$E_i=E_i^{\mathrm{band}}+E_i^{\mathrm{rep}}, \tag{2}$$

$$E_i^{\mathrm{band}}=-\sqrt{\sum_{j\neq i}\xi_{IJ}^2\exp\left[-2q_{IJ}\left(\frac{r_{ij}}{r_{IJ}^0}-1\right)\right]}, \tag{3}$$

$$E_i^{\mathrm{rep}}=\sum_{j\neq i}A_{IJ}\exp\left[-p_{IJ}\left(\frac{r_{ij}}{r_{IJ}^0}-1\right)\right], \tag{4}$$

where $r_{ij}$ is the distance between atoms at sites $i$ and $j$, respectively, occupied by the $I$ and $J$ chemical species ($I,J=\mathrm{Ag},\mathrm{Ni}$), and $r_{II}^0$ is the first-neighbor distance in the metal $I$ ($r_{IJ}^0=(r_{II}^0+r_{JJ}^0)/2$). The interactions in Eqs. (3) and (4) are

TABLE I. Parameters for the SMA potentials developed for this study and comparison with the experimental data (in parentheses). $A_{IJ}$ and $\xi_{IJ}$ are in eV. The experimental values for the lattice parameters $a$ (in Å) and for the cohesive energies $E_c$ (in eV/atom) are taken from Ref. 6; those for the elastic constants $B$, $C_{44}$, and $C'$ (in GPa) from Ref. 49.

| | $\xi_{IJ}$ | $A_{IJ}$ | $p_{IJ}$ | $q_{IJ}$ | $a$ | $E_c$ | $B$ | $C_{44}$ | $C'$ |
|---|---|---|---|---|---|---|---|---|---|
| Ni | 1.6396 | 0.1217 | 10.7626 | 2.4349 | 3.52 | −4.44 (−4.44) | 188 (188) | 100 (132) | 30 (55) |
| Ag | 1.2672 | 0.1249 | 10.3453 | 3.4236 | 4.09 | −2.95 (−2.95) | 108 (108) | 41 (51) | 14 (16) |

evaluated up to a distance $r_c$. To avoid discontinuities in both the energy and the forces, the hopping integrals $\xi$ and the repulsive interactions are connected to zero with a fifth-order polynomial between $r_c$ and a second cutoff distance $r_{c'}$. For this study, $r_c$ is chosen as $\sqrt{2}r_{IJ}^0$ and $r_{c'}$ is taken as $2r_{IJ}^0$ to obtain a smooth link if large distortions occur. For heteroatomic interactions, $r_c$ is taken as the second-neighbor distance of the element with the largest size, whereas $r_{c'}$ corresponds to the fourth-neighbor distance of the element with the smallest size.[45]

The energy depends on three sets of the four parameters ($\xi_{IJ}$, $A_{IJ}$, $p_{IJ}$, and $q_{IJ}$) which characterize the Ag-Ag, Ni-Ni, and Ag-Ni interactions. To describe pure metals, the fitting procedure is chosen to reproduce the energy for large distortions as well as possible. This is obtained by requiring that the energy of the perfect crystal lattice matches the universal binding curve of Rose *et al.*[49,50] This imposes the condition that cohesive energy, lattice parameter, and bulk modulus are strictly reproduced. Moreover, the calculation leads to correct values of the elastic constants (see Table I). The parameters describing the mixed Ni-Ag interaction have been adjusted in order to reproduce the large miscibility gap of this alloy, i.e., very weak solubility limits for the two solid solutions. The procedure consists in adjusting the Ni-Ag parameters on the enthalpies of mixing in the infinite dilution limit of the Ni (Ag) and Ag (Ni) solid solutions, the enthalpies of mixing being evaluated after relaxation. Then, the solubility limits are evaluated by Monte Carlo simulations with relaxations. Contrary to other bimetallic systems, the comparison between simulated and experimental solubility limits is not easy since there exist very few quantitative measurements for the Ni-Ag alloy. Therefore, we have verified the mixed Ni-Ag interatomic potential only on the solubility limit obtained at $T=773$ K in the Ni (Ag) solid solution,[51] which is the only quantitative experimental data for this system. As a result, the set of heteroatomic parameters is

$$A_{\text{Ni-Ag}} = 0.119 \text{ eV} \quad \text{and} \quad \xi_{\text{Ni-Ag}} = 1.412 \text{ eV}. \tag{5}$$

Note that, as usual, we have chosen an arithmetic average between the pure-metal values for $p_{\text{Ni-Ag}}$ and $q_{\text{Ni-Ag}}$ (see Ref. 48). In Table II, we report the resulting enthalpies of mixing and the solubility limits evaluated at $T=773$ K in the Ni(Ag) and Ag(Ni) solid solutions.

### C. Comparison between superstructures

We summarize the principles of the fast inertial relaxation engine (FIRE) method[53] used in this study, which is a recent development of the algorithm of quenched molecular dynamics that minimizes the potential energy at $T=0$ K.[54] The relaxation procedure consists in integrating the equation of motion for each atom of the simulation box,

$$\boldsymbol{F}_i(t) = m_i \frac{d\boldsymbol{v}_i(t)}{dt}, \tag{6}$$

where $\boldsymbol{v}_i(t)$ is the velocity at time $t$ of atom $i$ of mass $m_i$ and $\boldsymbol{F}_i(t)$ is the force acting on this atom at this time, calculated using the Verlet algorithm.[55] Then, the atom trajectories are adjusted by proposing two types of velocity changes: (i) cancellation of $\boldsymbol{v}_i$ when the product $\boldsymbol{F}_i(t)\cdot\boldsymbol{v}_i(t)$ is negative (equivalent to the classical quenched molecular-dynamics procedure[54]) and (ii) additional acceleration, $\gamma$, in the "steeper" directions than the direction at time $t$ if $\boldsymbol{F}_i(t)\cdot\boldsymbol{v}_i(t)>0$. This latter procedure is obtained by a simple linear combination between the global velocity ($3N$ dimensional) and the forces via $\boldsymbol{v}=(1-\alpha_v)\boldsymbol{v}+\alpha_v|\boldsymbol{v}|\frac{\boldsymbol{F}}{\|\boldsymbol{F}\|}$, where $\alpha_v = \gamma\Delta t$ and $\Delta t$ is the trajectory integration step; these two parameters being dynamically treated during the optimization procedure.[53] The force is calculated with the SMA potential described above and is simply obtained from

$$F_i = -\frac{dE_{\text{tot}}}{dr_i}, \tag{7}$$

with

$$E_{\text{tot}} = \sum_i E_i. \tag{8}$$

In practice, it is not possible to reach exactly $T=0$ K. Therefore, the simulations are stopped when $T<1.10^{-6}$ K, which ensures a precision on $E_{\text{tot}}$ better than 0.1 meV. Another problem may arise when one is interested in searching the lowest-energy minimum of such system (see, e.g., Ref. 56), as the number of local minima of the potential energy surface increases with the number of adsorbate atoms in the cell. To overcome possible trappings in relaxation procedure due to

TABLE II. Enthalpies of mixing $\Delta H^{\text{mix}}$ (expressed in eV/atom) and solubility limits $c_\alpha$ for the two solid solutions. The experimental data are reported in parentheses and are taken from Ref. 51 for $c_\alpha$ and from Ref. 52 for $\Delta H^{\text{mix}}$.

| | $\Delta H^{\text{mix}}$ | $c_\alpha$ (773 K) |
|---|---|---|
| Ni(Ag) | 0.70 (0.70) | $8\times10^{-5}$ ($1.5\times10^{-5}$) |
| Ag(Ni) | 0.58 (0.58) | $2.4\times10^{-4}$ |

the rigid construction of the simulation box, the system is thus allowed to relax following classical molecular dynamics during the first 20 steps.

Our goal is to compare the relative stabilities of the different possible superstructures for a Ag adlayer over a Ni(111) substrate by means of numerical simulations. Once the various superstructures have been generated following the Tkatchenko construction[33] and optimized via the relaxation FIRE algorithm,[53] one defines the most stable one as the structure which presents the minimum adsorption energy per Ag atom $E^{\mathrm{ads}}(\tau)$,[34]

$$E^{\mathrm{ads}}(\tau) = \frac{E_{\mathrm{tot}}(\tau) - E_{\mathrm{tot}}(\tau = 0)}{N_{\mathrm{Ag}}} - \mu_{\mathrm{Ag}}, \tag{9}$$

where $\tau = \frac{N_{\mathrm{Ag}}}{N_{\mathrm{Ni}}}$ is the interface density ratio [see Eq. (1)], $N_{\mathrm{Ag}}$ (respectively, $N_{\mathrm{Ni}}$) being the number of silver (respectively, nickel) atoms in the coincidence lattice, $E_{\mathrm{tot}}(\tau)$ is the total energy of the system for a given coverage, and $\mu_{\mathrm{Ag}}$ is the chemical potential of the Ag vapor phase. Note that the numerical value of $\mu_{\mathrm{Ag}}$ is not required here since $\mu_{\mathrm{Ag}}$ disappears when comparing two different coverages. In practice, we will set $\mu_{\mathrm{Ag}} = 0$.

## IV. RESULTS AND DISCUSSION

### A. Experimental results

The successive stages of the surface reconstruction as a function of the adsorbate coverage, growth temperature, and subsequent annealing have been identified through their LEED patterns (Fig. 1). In order to verify the good crystallographic order of the substrate and its orientation, LEED patterns of the clean (111) nickel surface were also recorded (not shown here).

After growth, performed either at room temperature or at 400 K, the silver deposit is poorly ordered and the additional spots on the LEED pattern are diffuse, especially for low silver coverages. In order to favor atomic diffusion, and therefore a better organization, the sample has been annealed at 525 K. The sharpening of the LEED pattern enabled an easier identification of the spots as shown in Fig. 1(a). The diffracted beams correspond to the epitaxial relationship, $\mathrm{Ag}(111)\|\mathrm{Ni}(111)$ with $\mathrm{Ag}[1\bar{1}0]\|\mathrm{Ni}[1\bar{1}0]$. We found a $(7\times7)$ reconstruction of the interface for all silver deposits (from 0.1 to 2.2 ML), corresponding to a coincidence lattice holding $N_{\mathrm{Ag}}=36$ silver atoms and $N_{\mathrm{Ni}}=49$ nickel atoms. The silver overlayer has then an in-plane lattice parameter close to its bulk value. Indeed, for a $(7\times7)$ reconstruction,

$$\frac{a_{\mathrm{Ag}}}{a_{\mathrm{Ni}}} = \sqrt{\frac{N_{\mathrm{Ni}}}{N_{\mathrm{Ag}}}} = \sqrt{\frac{49}{36}} = 1.167$$

and

$$\frac{a^b_{\mathrm{Ag}}}{a^b_{\mathrm{Ni}}} = \frac{4.09}{3.52} = 1.162,$$

with the bulk values.

After annealing the sample at 675 K, the LEED diffraction spots due to the silver layer are found rotated with respect to the substrate orientation, as can be seen in Fig. 1(c). A schematic of the LEED pattern is shown in Fig. 1(d), where the red dotted line illustrates the resulting orientation of the moiré structure and the $\theta$ angle according to the reconstruction nomenclature $(x\times x)R\theta$. We measured thus $\theta = (13.3\pm0.4)^\circ$. This rotation angle corresponds to a tilt angle $\alpha = -(2.4\pm0.4)^\circ$ between the Ag(111) and Ni(111) lattices at the interface, as illustrated by the green dotted line in Fig. 1(d). Moreover, the ratio between the Ni bulk derived lattice basis vector modulus and the reconstruction one is near 1/7 so that we can conclude that the coincidence lattice for this tilted reconstruction has a dimension close to $(7\times7)$. In some rare examples, different tilt angles with still lower values have also been observed, as shown in Fig. 1(b), obtained after Ag deposition of 1.2 ML at $T=525$ K. It should be mentioned that, in this sample a single domain reconstruction displayed in Fig. 1 has always been found whether in a few other cases, we have also observed two domain interfaces with the occurrence of $\pm\alpha$ diffraction spots.

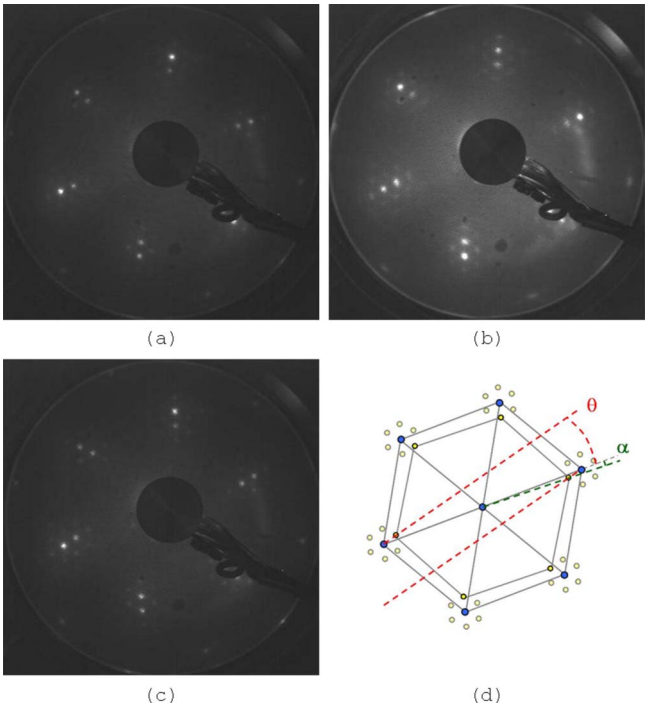


FIG. 1. (Color online) LEED pattern of Ni(111) surface, (a) after Ag deposition of 1.2 ML and annealing at $T=525$ K, (b) after Ag deposition at $T=525$ K of 1.2 ML, and (c) after annealing at $T=675$ K. Scheme (d) represents the LEED pattern (c), the red dotted line shows the angle $\theta$ in reconstruction $(x\times x)R\theta$ and the green dotted line shows the angle rotation $\alpha$ between Ag(111) and Ni(111) lattices.

### B. Geometry of Ag/Ni(111) tilted structures

In order to identify the coincidence lattices of the Ag/Ni(111) superstructures obtained in the present experiments, we have used the construction algorithm presented in Sec. III A.

The example of the collinear $(7\times7)$ superstructure is illustrated in Fig. 2(a), where only the interface between the

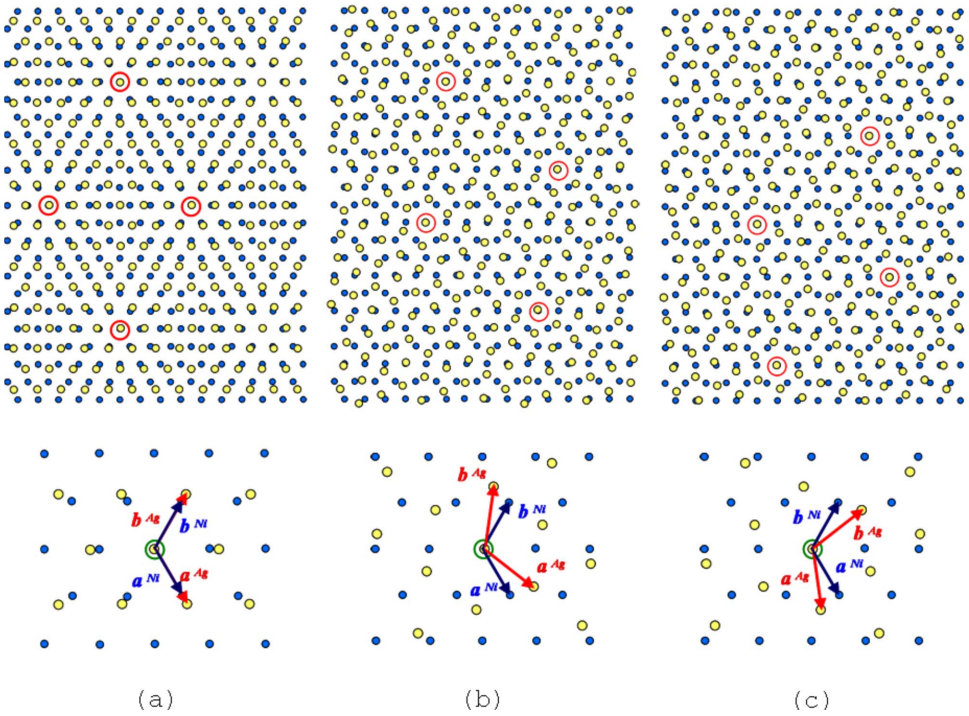


FIG. 2. (Color online) Coincidence lattices of hexagonal structures, silver is in yellow and nickel in blue: (a) $(7\times7)$ reconstruction [$N_{Ag}=36$ ($m_a=6$ and $n_a=0$) and $N_{Ni}=49$ ($m_s=7$ and $n_s=0$)], (b) and (c), respectively, $(7\times7)R\pm21.79°$ reconstructions with $\alpha=\pm21.79°$ [$N_{Ag}=36$ ($m_a=6$ and $n_a=0$) and $N_{Ni}=49$ ($m_s=8$ and $n_s=3$) and ($m_s=8$ and $n_s=5$)].

substrate top layer and the adsorbate first layer is represented. It shows clearly that the coincidence lattice holds 36 Ag atoms on top of 49 Ni atoms, with $\boldsymbol{A}_{Ag}=6\times\boldsymbol{a}_{Ag}$ and $\boldsymbol{A}_{Ni}=7\times\boldsymbol{a}_{Ni}$. With the same density ratio, we can also obtain the structures shown in Figs. 2(b) and 2(c), where we have fixed the silver superlattice to $\boldsymbol{A}_{Ag}=6\times\boldsymbol{a}_{Ag}$, but used two different supercells for the nickel substrate $\boldsymbol{A}_{Ni}=8\times\boldsymbol{a}_{Ni}+3\times\boldsymbol{b}_{Ni}$ and $\boldsymbol{A}_{Ni}=8\times\boldsymbol{a}_{Ni}+5\times\boldsymbol{b}_{Ni}$, which correspond, respectively, to rotations $\theta$ of $\pm21.79°$. These two reconstructions can be labeled $(7\times7)R\pm21.79°$ with a relative $\alpha=\pm21.79°$ between $\boldsymbol{a}_{Ag}$ (red arrow) and $\boldsymbol{a}_{Ni}$ (blue arrow) (in this particular case $\theta=\alpha=\pm21.79°$). The mirror symmetry relating the two tilted structures represented in Fig. 2 would disappear if more than one nickel layer were represented, indeed, when the actual substrate threefold symmetry is considered, the two reconstructions $(7\times7)R21.79°$ and $(7\times7)R-21.79°$ result *a priori* nonequivalent. The difference between the collinear and tilted interface atomic structures is readily apprehended by direct inspection of the figures and shows the importance of the rotation angle.

TABLE III. Adsorption energies ($E_{ads}$) in eV at$^{-1}$ calculated for a Ag monolayer (ML) and bilayer (BL) on Ni(111) surfaces and ranked by increasing interface density ratio $\tau$. Note that it is not possible to compare directly the values of $E_{ads}$ for a Ag monolayer to those of a Ag bilayer because of a variation in the chemical potential of the Ag vapor phase between these two configurations.

| Reconstruction | $N_{Ag}$ | $m_a$ | $n_a$ | $\theta_{Ag}$ (°) | $N_{Ni}$ | $m_s$ | $n_s$ | $\theta_{Ni}$ (°) | $\tau$ | $\alpha$ (°) | $E_{ads}$ (ML) | $E_{ads}$ (BL) |
|---|---|---|---|---|---|---|---|---|---|---|---|---|
| $(6\times6)$ | 25 | 5 | 0 | 0 | 36 | 6 | 0 | 0 | 0.694 | 0 | −3.161 | −3.025 |
| $(\sqrt{43}\times\sqrt{43})R7.59°$ | 31 | 6 | 1 | −8.95 | 43 | 7 | 1 | −7.59 | 0.721 | −1.36 | −3.173 | −3.042 |
| $(\sqrt{43}\times\sqrt{43})R7.59°$ | 31 | 6 | 5 | 8.95 | 43 | 7 | 1 | −7.59 | 0.721 | 16.54 | −3.161 | −3.037 |
| $(7\times7)$ | 36 | 6 | 0 | 0 | 49 | 7 | 0 | 0 | 0.735 | 0 | −3.176 | −3.047 |
| $(7\times7)R21.79°$ | 36 | 6 | 0 | 0 | 49 | 8 | 5 | −21.79 | 0.735 | 21.79 | −3.157 | −3.040 |
| $(\sqrt{52}\times\sqrt{52})R13.9°$ | 39 | 7 | 2 | −16.1 | 52 | 8 | 2 | −13.9 | 0.750 | −2.2 | −3.179 | −3.050 |
| $(\sqrt{52}\times\sqrt{52})R-13.9°$ | 39 | 7 | 5 | 16.1 | 52 | 8 | 6 | 13.9 | 0.750 | 2.2 | −3.179 | −3.050 |
| $(\sqrt{52}\times\sqrt{52})R13.9°$ | 39 | 7 | 5 | 16.1 | 52 | 8 | 2 | −13.9 | 0.750 | 30 | −3.164 | −3.040 |
| $(\sqrt{57}\times\sqrt{57})R6.59°$ | 43 | 7 | 1 | −7.59 | 57 | 8 | 1 | −6.59 | 0.754 | −1 | −3.178 | −3.049 |
| $(\sqrt{57}\times\sqrt{57})R6.59°$ | 43 | 7 | 6 | 7.59 | 57 | 8 | 1 | −6.59 | 0.754 | 14.18 | −3.168 | −3.045 |
| $(7\times7)R21.79°$ | 37 | 7 | 3 | −25.28 | 49 | 8 | 3 | −21.79 | 0.755 | −3.5 | −3.180 | −3.050 |
| $(7\times7)R21.79°$ | 37 | 7 | 4 | 25.28 | 49 | 8 | 3 | −21.79 | 0.755 | 47.1 | −3.170 | −3.046 |
| $(7\times7)$ | 37 | 7 | 3 | −25.28 | 49 | 7 | 0 | 0 | 0.755 | −25.28 | −3.154 | −3.041 |
| $(8\times8)$ | 49 | 7 | 0 | 0 | 64 | 8 | 0 | 0 | 0.766 | 0 | −3.176 | −3.048 |
| $(9\times9)$ | 64 | 8 | 0 | 0 | 81 | 9 | 0 | 0 | 0.790 | 0 | −3.164 | −3.035 |

Because of the divergence of the series leading to the possible structures via the construction algorithm, we restrict our study to configurations which are close to our experimental results in terms of supercell lattice parameters.

For a $(7\times7)$ reconstruction, we have a surface density ratio equal to

$$\tau = \frac{36}{49} = 0.735.$$

Note that for a bulklike heteroepitaxy between silver and nickel, we would expect

$$\frac{\sqrt{N_{\mathrm{Ag}}}}{\sqrt{N_{\mathrm{Ni}}}}\frac{a^b_{\mathrm{Ag}}}{a^b_{\mathrm{Ni}}} = 1$$

and

$$\tau^* = \frac{N_{Ag}}{N_{Ni}} = \left(\frac{a^b_{Ni}}{a^b_{Ag}}\right)^2 = 0.743.$$

Our experimental finding that the tilted reconstructed supercells has dimensions close to the $(7\times7)$ one led us to consider only structures which verify $\tau \simeq \tau^*$ and $N_{\mathrm{Ni}} \simeq 49$. We found five such couples of Ag and Ni atom numbers $N_{\mathrm{Ag}}$ and $N_{\mathrm{Ni}}$ leading to 11 different $\pm\alpha$ angles, reported in Table III.

Actually, under the same reconstruction label, $(x\times x)R\theta$, several possible superstructures can be built. For example, as shown in Table III, the reconstruction $(7\times7)R21.79°$ can be obtained in three different ways: with 36 silver atoms on top of 49 nickel atoms and $\alpha=21.79°$ between Ag(111) and Ni(111) lattice vectors (as in Fig. 2(b)) but also with 37 silver atoms on top of 49 nickel atoms and $\alpha=-3.5°$ or $\alpha=-12.93°$. Indeed, the above nomenclature only takes into account the substrate coincidence lattice dimension ($N_{\mathrm{sub}}=x^2$) and the orientation of the moiré structure ($\theta=-\theta_{\mathrm{Ni}}$), which is not sufficient to fully describe a tilted superstructure. Each superstructure has also to be referred to the number of adsorbate atoms ($N_{\mathrm{ads}}$) and the tilt angle ($\alpha=\theta_{\mathrm{Ag}}-\theta_{\mathrm{Ni}}$).

### C. Energetics of Ag/Ni(111)

Following the simulation procedure described in Sec. III C, we have calculated the adsorption energies for all the selected superstructures (see Table III). Those adsorption energies were calculated both for a Ag(111) monolayer and for a Ag(111) bilayer adsorbed on the Ni(111) substrate since the latter was found more stable even in the very early stages of growth.[21] Note that the number of substrate planes included in the simulations has been systematically optimized to obtain convergence of the calculation. In Table III, only the calculated adsorption energies for the case of $\theta$ positive are reported. Indeed, the calculation cannot discriminate between both rotation directions of the silver lattice on the nickel substrate. See, for example, the value of the calculated adsorption energy for the two reconstructions $(\sqrt{52}\times\sqrt{52})R\pm13.9°$ (with $N_{\mathrm{ads}}=39$ and $\alpha=\mp2.2°$), reported in Table III. However, in most cases, only one domain is experimentally observed by LEED, i.e., one sign for $\theta$ and $\alpha$ angles (see Figs. 1(c) and 1(d)). Therefore, this predominance should be ascribed to extrinsic parameters not taken into account in the calculation, such as the direction and density of steps on the substrate and the deposition or annealing temperatures among others.

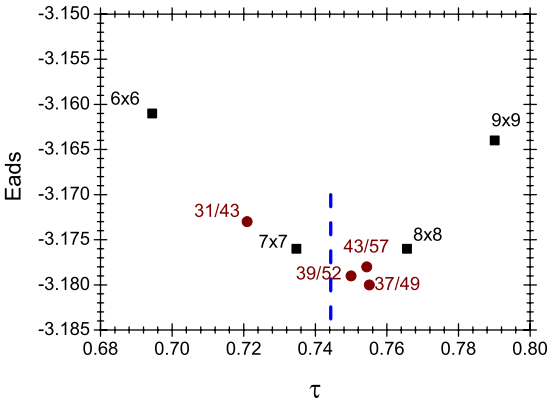


FIG. 3. (Color online) $E_{\mathrm{ads}}=f(\tau)$ for a silver monolayer adsorbed on Ni(111) substrate, the blue dotted line corresponding to the bulk parameter ratio between Ag and Ni.

Before discussing further the results of the simulations, let us outline that the adsorption energy values displayed in Table III are given per adsorbate atom and have a significance better than 1 meV. The main result is that, for a same interface density ratio $\tau$, the most favorable reconstruction is obtained for the smallest absolute value of the tilt angle $\alpha$. Figures 3 and 4 display the lowest adsorption energies as a function of $\tau$ for a Ag monolayer and bilayer, respectively. Those graphs reveal that the minimum of adsorption energy is found for a density ratio $\tau$ close to the bulk parametric match $\tau^*$. Moreover, in both cases, three of the tilted reconstructions are found more favorable than the collinear $(7\times7)$: the $(\sqrt{52}\times\sqrt{52})R13.9°$ (with $N_{\mathrm{ads}}=39$ and $\alpha=-2.2°$), the $(7\times7)R21.79°$ (with $N_{\mathrm{ads}}=37$ and $\alpha=-3.5°$), and the $(\sqrt{57}\times\sqrt{57})R6.59°$ (with $N_{\mathrm{ads}}=43$ and $\alpha=-1°$). However, after silver deposit and annealing at moderate temperatures (525 K in the present experiment), the $(7\times7)$ reconstruction is observed, as was also mentioned in the published literature.[7,9,12] From these calculations, we can thus deduce that this interface state is metastable. This is confirmed by

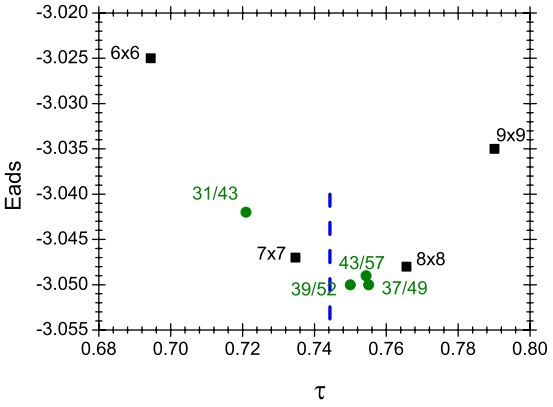


FIG. 4. (Color online) $E_{\mathrm{ads}}=f(\tau)$ for a silver bilayer adsorbed on Ni(111) substrate, the blue dotted line corresponding to the bulk parameter ratio between Ag and Ni.

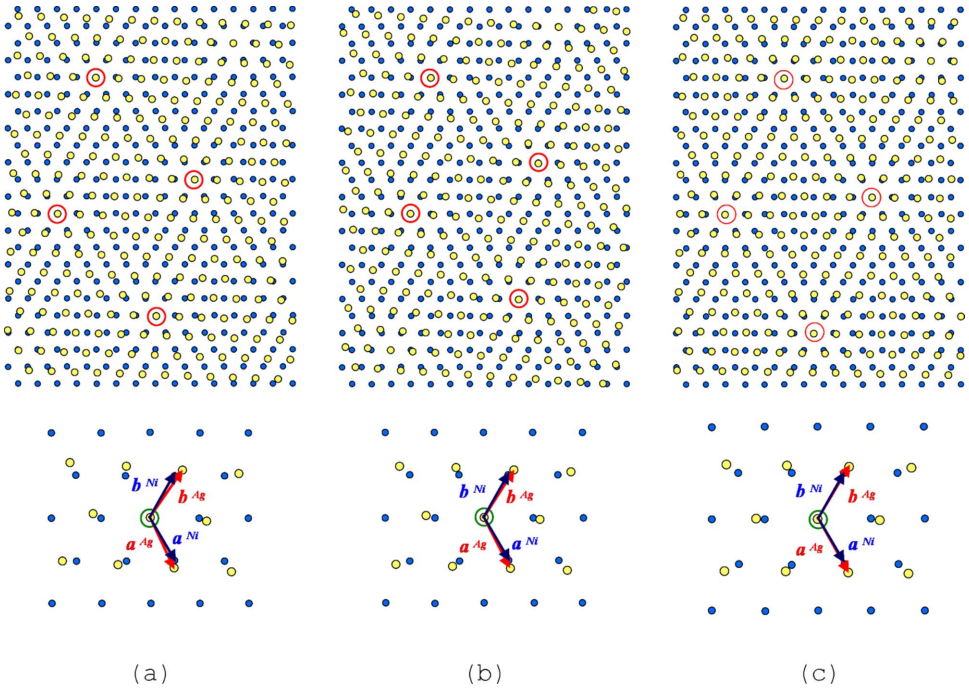


FIG. 5. (Color online) Coincidence lattices of favorable hexagonal structures, silver is in yellow and nickel in blue: (a) $(\sqrt{52}\times\sqrt{52})R13.9°$ reconstruction with $\alpha=-2.2°$ [$N_{Ag}=39$ ($m_a=7$ and $n_a=2$) and $N_{Ni}=52$ ($m_s=8$ and $n_s=2$)], (b) $(7\times7)R21.79°$ reconstruction with $\alpha=-3.5°$ [$N_{Ag}=37$ ($m_a=7$ and $n_a=3$) and $N_{Ni}=49$ ($m_s=8$ and $n_s=3$)] and (c) $(\sqrt{57}\times\sqrt{57})R6.59°$ with $\alpha=-1°$ [$N_{Ag}=43$ ($m_a=7$ and $n_a=1$) and $N_{Ni}=57$ ($m_s=8$ and $n_s=1$)].

our STM observations which show a significant modification of the overlayer organization after annealing at 675 K,[21] corresponding to the apparition of the tilted reconstruction. After this last annealing, the silver only forms bilayer on the Ni surface. For a Ag bilayer, the three favorable tilted reconstructions are almost energetically degenerate with $E_{ads}=-3.050$ eV at$^{-1}$ or $-3.049$ eV at$^{-1}$. The construction of the three superlattices is illustrated (with only one silver layer for the sake of clarity) in Fig. 5. A quick inspection of the figure shows that the geometry of the three coincidence lattices in terms of atomic distribution across the interface is very similar, contrary to the geometry of the structures shown in Fig. 2. This feature could explain the very small difference between the three calculated adsorption energies. In order to put figures on this intuitive perception and compare the built-in strain in the different interfaces, the nearest-neighbors interatomic distances have been calculated for the optimized $(7\times7)$ reconstruction and the tilted ones. The average values within each silver layer, labeled Ag1-Ag1 and Ag2-Ag2, and in between both layers, labeled Ag1-Ag2, are displayed in Fig. 6. The in-plane average value is directly linked to the density ratio $\tau$, and indeed, the largest tensile in-plane strain is observed for the $(7\times7)$, whereas the out-of-plane strain is accordingly compressive for this interface. Concerning the tilted reconstructions, the average strains are much smaller than for the collinear one, and moreover, two of them, the $(7\times7)R21.79°$ and the $(\sqrt{57}\times\sqrt{57})R6.59°$ do not show any trigonal distortion. However, the interpretation is not so straightforward since all strains are found compressive with respect to an ideally relaxed bulk value. A tentative explanation could be that for such a thin layer, the equilibrium parameter is reduced and could be close to the one adopted by the two undistorted interfaces, the third reconstructed interface, $(\sqrt{52}\times\sqrt{52})R13.9°$, showing then a slight trigonal distortion. In any case, the average distances found for the three tilted reconstructions are very similar.

### D. Comparison with the experimental data

The reconstruction observed on the LEED patterns after annealing at 675 K can be written as $(x\times x)R13.3\pm0.4°$, with $x\simeq\sqrt{49}$ and $\alpha=-(2.4\pm0.4)°$. By comparing this to the $\theta$ and $\alpha$ parameters of the three reconstructions energetically favored, we found that the $(\sqrt{52}\times\sqrt{52})R13.9°$ with $N_{ads}=39$ and $\alpha=-2.2°$ shows the best agreement with our experimental results. Moreover, the same Ag/Ni(111) reconstruction with the same rotation of the silver lattice has been already observed on STM moiré images with atomic resolution by Vang *et al.*[20] and LEED results obtained by Feinstein *et al.*,[7] Meinel *et al.*,[9] and Mróz *et al.*[12] also display tilted reconstructions with $\alpha=\pm2.2°$ or $\alpha=\pm2.3°$ between

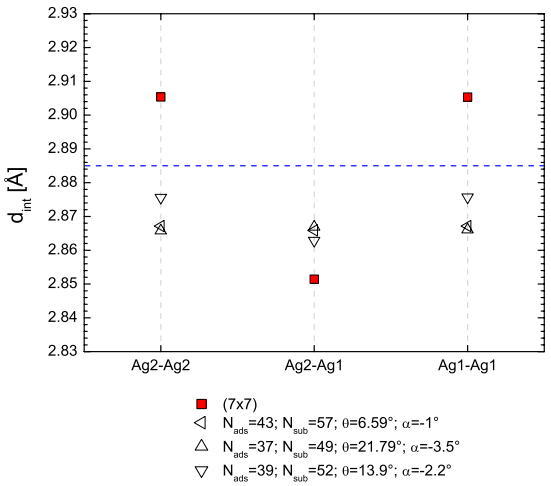


FIG. 6. (Color online) Average first-neighbor distances, expressed in Å, within each silver layer, labeled Ag1-Ag1 (interface layer) and Ag2-Ag2, and in-between both layers, labeled Ag1-Ag2. The blue dotted line corresponding to the silver bulk first-neighbor distance.

Ag and Ni lattices. So, we can conclude that the structure we observe by LEED after an annealing at 675 K is a $(\sqrt{52} \times \sqrt{52})R13.9°$ reconstruction. The other reconstruction close to the energy minimum, the $(\sqrt{57} \times \sqrt{57})R6.59°$ one, has indeed been observed on a STM moiré pattern by Besenbacher *et al.*[19] and is also present in some of our own LEED data [Fig. 1(b)]. These independent experimental results clearly demonstrate the validity of our simulation procedure that exhibits several reconstructions degenerate in energy.

## V. CONCLUSION

In this paper, we have used atomic-scale simulations with realistic *N*-body potentials derived from the electronic structure to place the Ag/Ni(111) possible reconstructions on a robust comparative energy scale. The results have been confronted to the available experimental data and have provided a very satisfactory interpretation of the main observations. In particular, the phase transition between the collinear $(7 \times 7)$ and the $(\sqrt{52} \times \sqrt{52})R13.9°$ tilted reconstruction observed by LEED after annealing at 675 K and also in published STM data has been fully accounted for since it is one of the few tilted reconstructions identified by the simulations as more stable than the collinear $(7 \times 7)$. The success of the method in selecting the reconstructed interfaces actually found experimentally relies on a proper description of the interaction between the adlayer and substrate which induces deformations down to more than ten layers and appears thus as the driving force for reconstruction. However, further studies are needed to better understand the hierarchy of the reconstructions as a function of the temperature. Among all, an evaluation of the Gibbs-free energy, by adding the contribution of the vibrational entropy, should lift the degeneracy in internal energy since vibrational entropy is closely linked to the stress rate near the surface plane,[35] which is not strictly the same for the different reconstructions.

## ACKNOWLEDGMENTS

The authors thank Bernard Legrand and Isabelle Braems for very fruitful discussions.

[1] J. A. Venables, G. D. T. Spiller, and M. Handbrucken, Rep. Prog. Phys. **47**, 399 (1984).
[2] E. Bauer and J. H. van der Merwe, Phys. Rev. B **33**, 3657 (1986).
[3] E. Bauer, Appl. Surf. Sci. **11–12**, 479 (1982).
[4] T. Surholt, C. Minkwitz, and C. Herzig, Acta Mater. **46**, 1849 (1998).
[5] Z. C. Li, D. P. Yu, and B. X. Liu, Phys. Rev. B **65**, 245403 (2002).
[6] C. Kittel, *Introduction to Solid State Physics*, 7th ed. (Wiley, New York, 1995).
[7] L. G. Feinstein, E. Blanc, and D. Dufayard, Surf. Sci. **19**, 269 (1970).
[8] D. C. Jackson, T. E. Gallon, and A. Chambers, Surf. Sci. **36**, 381 (1973).
[9] K. Meinel, O. Lichtenberger, and M. Klaua, Phys. Status Solidi A **116**, 47 (1989).
[10] S. Mróz and Z. Jankowski, Surf. Sci. **322**, 133 (1995).
[11] S. Mróz, M. Nowicki, and Z. Jankowski, Prog. Surf. Sci. **53**, 197 (1996).
[12] S. Mróz and Z. Jankowski, Surf. Sci. **454-456**, 702 (2000).
[13] T. Ito, K. Umezawa, and S. Nakanishi, Appl. Surf. Sci. **130-132**, 497 (1998).
[14] A. P. Shapiro, T. Miller, and T.-C. Chiang, Phys. Rev. B **37**, 3996 (1988).
[15] A. P. Shapiro, T. C. Hsieh, A. L. Wachs, T. Miller, and T.-C. Chiang, Phys. Rev. B **38**, 7394 (1988).
[16] S. Smadici, D. Mocuta, and R. M. Osgood, Phys. Rev. B **69**, 035415 (2004).
[17] A. Varykhalov, A. M. Shikin, W. Gudat, P. Moras, C. Grazioli, C. Carbone, and O. Rader, Phys. Rev. Lett. **95**, 247601 (2005).
[18] K. Umezawa, T. Ito, S. Nakanishi, and W. M. Gibson, Appl. Surf. Sci. **219**, 102 (2003).
[19] F. Besenbacher, L. P. Nielsen, and P. T. Sprunger, in *The Chemical Physics of Solid Surfaces*, edited by D. A. King and D. P. Woodruff (Elsevier, New York, 1997), Vol. 8, Chap. 6.
[20] R. T. Vang, K. Honkala, S. Dahl, E. K. Vestergaard, J. Schnadt, E. Lægsgaard, B. S. Clausen, J. K. Nørskov, and F. Besenbacher, Surf. Sci. **600**, 66 (2006).
[21] C. Chambon, A. Coati, and Y. Garreau, Surf. Sci. **602**, 2363 (2008).
[22] G. S. Leatherman and R. D. Diehl, Phys. Rev. B **53**, 4939 (1996).
[23] G. S. Leatherman, R. D. Diehl, M. Karimi, and G. Vidali, Phys. Rev. B **56**, 6970 (1997).
[24] C. A. Lucas, N. M. Marković, and P. N. Ross, Phys. Rev. B **55**, 7964 (1997).
[25] S. Terada, T. Yokoyama, N. Saito, Y. Okamoto, and T. Ohta, Surf. Sci. **433-435**, 657 (1999).
[26] M. Caragiu, G. S. Leatherman, Th. Seyller, and R. D. Diehl, Surf. Sci. **475**, 89 (2001).
[27] S. Haq, J. Harnett, and A. Hodgson, Surf. Sci. **505**, 171 (2002).
[28] A. D. Novaco and J. P. McTague, Phys. Rev. Lett. **38**, 1286 (1977).
[29] J. P. McTague and A. D. Novaco, Phys. Rev. B **19**, 5299 (1979).
[30] D. L. Doering, J. Vac. Sci. Technol. A **3**, 809 (1985).
[31] F. Grey and J. Bohr, Europhys. Lett. **18**, 717 (1992).
[32] A. Tkatchenko, Phys. Rev. B **74**, 035428 (2006).
[33] A. Tkatchenko, Phys. Rev. B **75**, 235411 (2007).
[34] C. Mottet, G. Tréglia, and B. Legrand, Phys. Rev. B **46**, 16018 (1992).
[35] I. Meunier, G. Tréglia, R. Tétot, J. Creuze, F. Berthier, and B. Legrand, Phys. Rev. B **66**, 125409 (2002).
[36] Y. Garreau, A. Coati, A. Zobelli, and J. Creuze, Phys. Rev. Lett. **91**, 116101 (2003).
[37] A. Coati, J. Creuze, and Y. Garreau, Phys. Rev. B **72**, 115424 (2005).

[38] V. Rosato, M. Guillopé, and B. Legrand, Philos. Mag. A **59**, 321 (1989).
[39] F. Ducastelle, J. Phys. (Paris) **31**, 1055 (1970).
[40] M. Guillopé and B. Legrand, Surf. Sci. **215**, 577 (1989).
[41] F. Berthier, B. Legrand, and G. Tréglia, Acta Mater. **47**, 2705 (1999).
[42] J. Creuze, F. Berthier, R. Tétot, and B. Legrand, Surf. Sci. **491**, 1 (2001).
[43] J. Creuze, F. Berthier, R. Tétot, and B. Legrand, Surf. Sci. **491**, L651 (2001).
[44] R. Tétot, F. Berthier, J. Creuze, I. Meunier, G. Tréglia, and B. Legrand, Phys. Rev. Lett. **91**, 176103 (2003).
[45] F. Berthier, B. Legrand, and G. Tréglia, Interface Sci. **8**, 55 (2000).
[46] J. Creuze, F. Berthier, R. Tétot, and B. Legrand, Phys. Rev. Lett. **86**, 5735 (2001).
[47] J. Creuze, Defect Diffus. Forum **203-205**, 3 (2002).
[48] G. Tréglia and B. Legrand, in *Tight-Binding Approach to Computational Materials Science*, MRS Symposia Proceedings No. 491 (Materials Research Society, Pittsburgh, 1998), p. 275.
[49] J. H. Rose, J. R. Smith, F. Guinea, and J. Ferrante, Phys. Rev. B **29**, 2963 (1984).
[50] D. Spanjaard and M. C. Desjonquères, Phys. Rev. B **30**, 4822 (1984).
[51] S. Taoud, Ph.D. thesis, Université de Nantes, Nantes, France, 1989.
[52] R. Hultgren, P. D. Desay, D. T. Hawkins, M. Gleiser, K. K. Kelley, and D. D. Wagman, *Selected Values of the Thermodynamic Properties of Metals and Binary Alloys* (Wiley, New York, 1973).
[53] E. Bitzek, P. Koskinen, F. Gahler, M. Moseler, and P. Gumbsch, Phys. Rev. Lett. **97**, 170201 (2006).
[54] C. H. Bennett, in *Diffusion in Solids, Recent Developments*, edited by A. S. Nowicki and J. J. Burton (Academic, New York, 1975), p. 73.
[55] L. Verlet, Phys. Rev. **159**, 98 (1967).
[56] A. Tkatchenko, Phys. Rev. B **75**, 085420 (2007).